5

RESOLVING MEMBRANE-BOUND PROTEIN ORIENTATION AND CONFORMATION BY NEUTRON REFLECTIVITY

Hirsh Nanda

High-resolution structural characterization of membrane-bound proteins is itself a significant challenge but only provides part of our understanding with regards to function. The spatial organization of these proteins with respect to the lipid membrane is also important for their activity in biological processes. However, information such as the binding orientation of peripheral membrane proteins, conformational changes in integral proteins, and subunit organization of protein complexes are often lacking in high-resolution structures. Because biological membranes are thermally disordered environments, noncrystallographic scattering approaches are required. X-ray and neutron reflectivity have been applied in the past to characterize thin fluid films at the subnanometer level. Lately, neutron reflectivity (NR) has emerged as a powerful tool to study the complex molecular architecture of biological membrane systems. This has required the development of biomimetic lipid membrane environments, enhanced experimental methods, and sophisticated data analysis. One particularly important advancement has been the integration of high-resolution data and molecular modeling with NR to yield a 3D view of proteins on the membrane. In this chapter, these methods will be reviewed and examples in HIV-1 viral assembly will be given. Future strategies, employing selective deuteration and combining constraints from multiple membrane-protein methods, will also be discussed. Understanding the molecular forces that govern the structure and function of membrane proteins requires the continued development of new metrologies. Eventually, such insights can be used toward engineering test beds for therapeutic agents and applications in surface functionalization, biosensors, or self-assembly of biologically inspired nanoparticles.

5.1 INTRODUCTION

Structural biology has played a critical role in advancing biomedical research at the molecular level. However, some important classes of functional biomolecular assemblies, such as membrane proteins, pose persisting challenges to traditional characterization methods. Nearly one third of the human genome codes for membrane-associated proteins, some with vital roles in cellular function, such as cell signaling [1], respiration [2], and protein expression [3]. On the other hand, some viral pathogens direct the formation of new infectious virions on the host cell plasma membrane [4]. Important questions regarding how these proteins target the membrane, change their structure, or interact with other proteins, and ultimately give rise to health and disease, are largely unresolved.

A number of diverse methods have been brought to bear on membrane-protein systems, underlining both their importance and difficulty of study. Techniques such as atomic force microscopy [5], electron paramagnetic resonance [6], solution and solid-state NMR [7], electron microscopy [8] as well as X-ray crystallography [9] have provided structural information at varying resolutions. Important additions to this list are neutron [10] and X-ray reflectivity [11]. These techniques are exquisitely sensitive to structure at interfacial surfaces (e.g., lipid membranes) and are able to characterize thermally disordered and fluid bilayers—the physiologically relevant protein environment.

The nature of neutron interactions with atoms has made neutron reflectivity (NR) a particularly advantageous technique for biological systems. A chief characteristic is the contrast in scattering intensity between hydrogen

Proteins in Solution and at Interfaces: Methods and Applications in Biotechnology and Materials Science, First Edition. Edited by Juan M. Ruso and Ángel Piñeiro.

and deuterium isotopes. Isomorphic replacement provides a noninvasive probe allowing specific structures within a molecular complex to be highlighted. Furthermore, "contrast variation" of aqueous buffers consisting of different H_2O/D_2O mixtures indirectly incorporates phase information during model refinement confirming unique solutions and improving our spatial resolution in our structure determinations. As opposed to X-rays, prolonged exposure to a neutron beam does not degrade soft-matter biological samples; hence, multistep experiments can be designed and protein conformation changes in response to interactions with cofactors observed *in situ.*

The intent of this chapter is to highlight several years of developing the capabilities of NR in the molecular-level characterization of membrane-protein structure. We will begin with a brief overview of the practical aspects of reflectivity and model membrane systems used as a platform for membrane protein study. The interpretation of reflectivity data using advanced models and sophisticated analysis methods will then be presented. The remaining chapter will use recent work on HIV-1 viral assembly proteins to demonstrate how integrating high-resolution structures into our reflectivity refinement procedures resolves molecular details of protein penetration and orientation on the membrane. We further will show evidence that interactions with the membrane and other cofactors can result in conformational changes to membrane-bound proteins relevant to their biological function. The methods described here have a broad based application to protein adsorption to all interfacial surfaces including surfactant, polymer, and solid interfaces with potential applications in pharmaceutical and biomaterials research.

5.2 SPECULAR REFLECTIVITY

In reflectivity experiment, a planar neutron beam is reflected off a thin film or surface at low grazing incidence angles. The ratio of the intensity of the reflected beam to the intensity of the incident beam measured at the same grazing angle is the specular reflectivity ($R = I_r/I_o$). Figure 5.1 is a schematic of typical reflection measurement geometry, showing the incident beam, I_o, reflecting from a solid supported membrane film at an angle, θ, from the surface. Analysis of the data provides structural information in terms of a 1D profile along the axis normal to the surface. This profile depends on the density and chemical composition of different molecular groups in the surface normal direction (z-axis) and is referred to as the neutron scattering length density (nSLD or SLD).

Reflection is measured as a function of increasing grazing angle between the incident and the reflected beam until background noise dominates the reflection signal. At these low angles neutrons penetrate the film surface by a ~1000 Angstroms. Therefore, neutrons that reflect off buried interfaces (e.g., lipid, water, or protein layers in the case of a membrane film) interfere both constructively and destructively, modulating the reflected intensity as a function of angle. The nature of the interference patterns depends on the molecular architecture of the interfacial structure. In plane, structure or heterogeneity is effectively averaged in specular reflection assuming these structures are smaller than the neutron coherence length, ~1–10 μm.

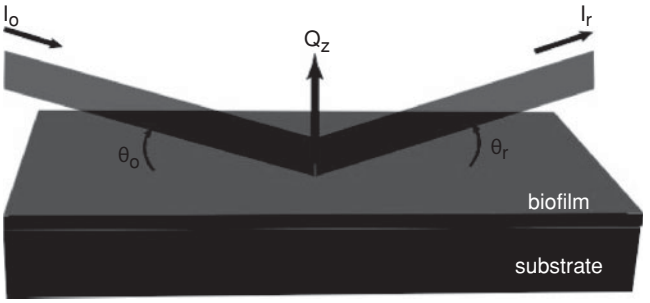

FIGURE 5.1 Reflectivity measurement geometry. A flat well-collimated neutron beam, I_o, sub-millimeter thin in z is incident upon the membrane film at grazing angle θ_o. Reflection occurs at all interfaces within the film as well as with the underlying substrate layer and the reflected intensity, I_r, is measured at θ_r. For specular reflection ($\theta_o = \theta_r$), only the Q_z component of the momentum transfer in the reflected beam changes. A bulk aqueous environment is used above the film and often the sample is flipped such that the neutron beam first travels through the solid substrate layer reflecting from the back of the film layer.

For a perfectly smooth and flat surface that is also homogenous (no in-plane structure), reflection can only be specular, that is, the momentum transfer, Q, between the incident and the reflected neutron beam can only occur normal to the membrane plane. Thus, as evident in Figure 5.1, there is a straightforward geometric relationship between the normal Q vector, Q_z, and the angle of incidence.

$$Q_z = \frac{4\pi}{\lambda} \sin\theta, \tag{5.1}$$

where λ is the wavelength of the neutron beam (typically 2–14 Å depending on the source). Real surfaces have molecular scale roughness and in-plane heterogeneity leading to reflection at angles off the incidence angle, $\pm\Delta\theta$, defined as off-specular scattering. Interpretation of the off-specular scattering in terms of the in-plane structure is still a newly developing area [12, 13] and is not the focus of this chapter. However, off-specular scattering does contribute to the background of the specular signal and must be measured for proper background subtraction.

The highest real-space resolution attainable for the molecular structure in our membrane films is ultimately dependent on the maximum momentum transfer, $Q_{z,max}$, for which specular reflectivity signal can be measured. Fresnel's equation

shows that reflected intensity drops in relation to Q^4, such that at Q values ≈ 0.3 Å the reflected intensity may already fall between 10^{-6} and 10^{-8} and close to background levels. Therefore, increasing resolution can generally be accomplished in two ways: increasing the intensity of the incident neutron beam or reducing background. The first factor is generally constrained by the neutron scattering facility. However, the latter can very much depend on sample and instrument setup. For example, samples with high molecular roughness will result in increased off-specular scattering raising the background and reducing the specular intensity. Curvature on the macroscopic length scale will also reduce allowable resolution. Furthermore, scattering from air or hydrogenous material within the sample (particularly large aqueous reservoirs) results in increased incoherent scattering, another major source of background. In one experiment, optimization of these factors allowed a $Q_{z,max}$ of 0.7 Å^{-1} to be reached showing detail of melittin peptide interacting with a membrane layer [14]. Typical values fall well below 0.3–0.5 Å^{-1}, resulting in real-space resolution of 5–10 Å using the relationship $l = \pi/Q_{z,max}$ [15, 16].

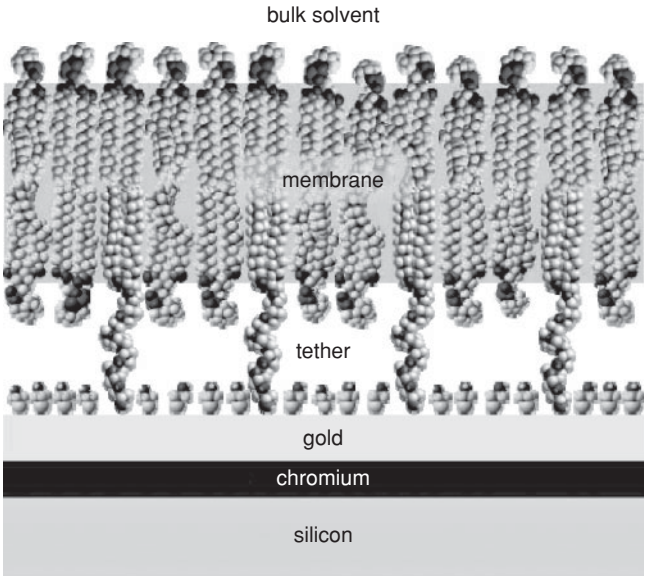

FIGURE 5.2 Cartoon schematic of a tethered membrane system used for incorporating membrane proteins in neutron reflectivity measurements.

5.3 TETHERED BILAYERS

For reflectivity measurements, membrane preparations are required to have flat planar geometries and remain defect free over surface areas of a few square centimeters. Several model membrane systems that satisfy these criteria have been used with great success. Many early measurements focused on protein adsorption to lipid monolayers at the air–water interface [17–20] in Langmuir trough apparatuses. This system is still highly informative today providing unique complimentary information such as the molecular volume of the protein groups that insert into the lipid layer and the insertion pressures associated with them. However, for transmembrane proteins monolayers are not a suitable model for the lipid bilayer environment.

The deposition of solid supported membranes on hydrophilic or hydrophobic surfaces is another common biomembrane mimic. These preparations can take many forms and generally have the advantage of providing highly stable membrane layers for protein incorporation. Defect-free membranes are easily formed with hybrid membranes, where a lipid layer is deposited onto an immobilized alkane layer [21], and proteins and peptides that are monotopic can be studied [22]. Lipid bilayers can be formed on polished silicon wafers with hydrophilic silicon oxide films or quartz slide surfaces which strongly physisorb zwitterionic headgroups [23, 24]. However, coupling to the solid substrate may still alter lipid packing and phase behavior and provide an insufficient submembrane space for the hydrophilic domains of transmembrane proteins [24]. For these systems, Langmuir–Blodgett [25], vesicle fusion, and even rapid solvent exchange [26] have been effective methods for membrane deposition.

Strategies to decouple the membrane from the underlying substrate have generally taken two forms: polymer-cushioned and polymer-tethered membranes. As the name implies, an intervening polymer layer softens the coupling to the hard surface in polymer-cushioned membranes. Neutron reflectivity measurements have shown aqueous reservoirs between the membrane and the polymer, important for transmembrane proteins [27–29]. It is important for these systems to control the roughness of the polymer surface, as a high interfacial roughness can negatively impact structural resolution.

For our investigations, tethered bilayers have proven to be an excellent biomimetic membrane model [30,31] capable of incorporating functional peripheral and transmembrane proteins [26, 32, 33]. Development and characterization by our group and others have resulted in a well-controlled system, where composition of a diversity of lipid species can be modulated. Figure 5.2 shows a schematic of the tethered system. As seen, a synthetic lipid with a built-in molecular spacer sparsely covers the substrate surface bound by thiol chemistry to a thin Au layer. The tethering compound nucleates membrane assembly while the PEO spacer ensures a $\sim$2 nm thin water reservoir between the membrane and the Au. Capping the Au layer with BME stabilizes it on the aqueous side while Cr is used to bond the Au to the Si substrate. Finally accessibility to the bulk solvent phase allows the introduction of proteins or other biochemical factors *in situ*, during experiments.

The sparsely tethered lipid membrane (stBLM) provides us with many desirable properties. The deposited lipid membranes form with low atomic roughness (∼3 Å), allowing for higher resolution measurements. Separation of the membrane from the solid substrate promotes lipid fluidity [34]. The tether also improves membranes resiliency allowing for multiple solvent contrast exchanges and multiple structural measurements on a given preparation. Finally, the underlying Au film makes the system amenable to complimentary methods such as SPR for measuring protein-binding thermodynamics and kinetics and EIS for measuring the function of incorporated ion channels. By performing these measurements *in situ* with reflectivity, direct correspondence with protein structure can be achieved.

5.4 MODELING DATA

5.4.1 Modeling Tethered Bilayers

Data interpretation of reflectivity measurements generally requires the use of real-space models of the nSLD profile that are adjusted to fit the reflectivity results. The direct determination of the nSLD profile is prohibited by the "phase problem," common to scattering techniques. That is, we are only sensitive to changes in the absolute intensity, $R = |r|\exp(i\phi)|r|\exp(-i\phi)$, losing information on the phase angle ϕ of the reflected beam. The lack of phase can introduce additional ambiguities in the uniqueness of a SLD model to the reflectivity spectra. Recent developments in theory and experiment demonstrated the use of phase-sensitive scattering to recover phase angle information [16, 35, 36], allowing for "direct inversion" or model-free determination of the SLD profile. Magnetic reference layers or surround media variation techniques were used in these experiments.

Modeling approaches, however, can also circumvent the "phase problem" through contrast variation of the aqueous buffer. In this approach, the aqueous buffer is exchanged with different H_2O/D_2O mixtures and reflectivity measurements are taken for each contrast condition. The unique reflectivity profiles all report on the same underlying molecular architecture of the membrane-protein film allowing one consistent model to be simultaneously fit to the independent reflectivity spectra. In addition a priori knowledge on the ordering of the Si/SiOx/Cr/Au substrate films provides additional constraints to data interpretation. This indirect incorporation of phase information ensures uniqueness in the fit SLD profiles.

The representation of thin film structures normal to the membrane plane requires models with quantitative parameters for fitting the reflectivity data. Perhaps the simplest but still highly informative are "box" or strip models [37, 38]. In such a representation, layers divide the film into chemically or structurally distinct regions, such as lipid hydrocarbon, headgroups, or the underlying Au metal film. Each region is then considered a homogenous slab of planar cross-section and of constant scattering length density. Slabs are layered along the membrane normal, thereby defining the 1D SLD profile.

Comparison to experimental data is done using Parratt's recursion algorithm [39] for computing the reflectivity profile from multiple slab layers. An iterative fitting procedure is used where box model parameters are adjusted until the fit to the reflectivity data converges. Ultimately, reflectivity is a function of the underlying SLD profile, where any complex density distribution can be arbitrarily divided into any number of thin layers and the resulting reflectivity spectra calculated. This will prove to be highly useful for modeling protein structures as seen in later sections.

An example of reflectivity data measured on a tBLM containing DMPC lipids is shown in Figure 5.3a. The neat membrane layer was measured in aqueous buffers of three

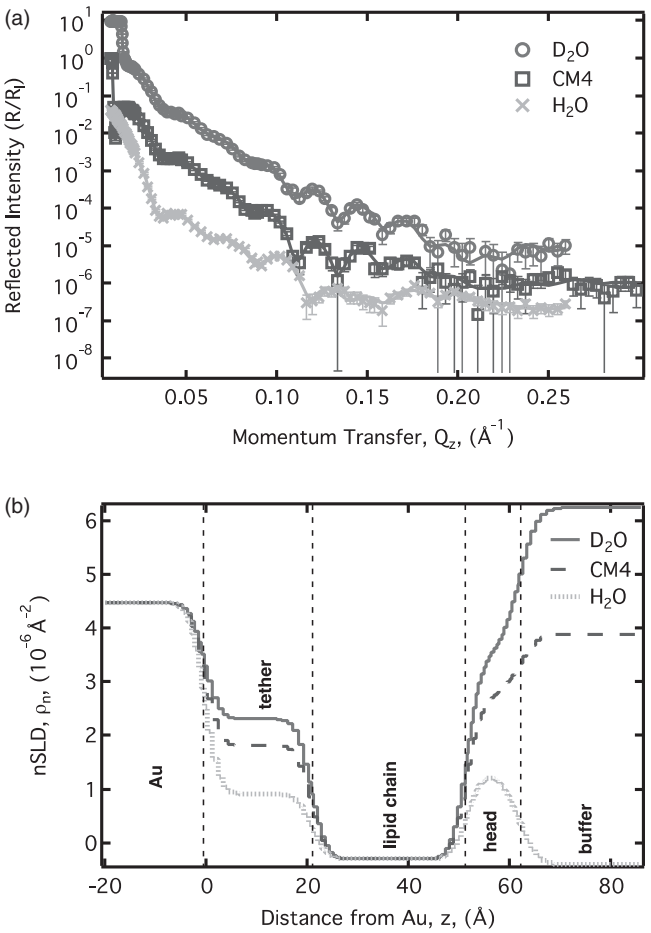

FIGURE 5.3 Structural characterization of a stBLM formed with DMPC lipids deposited by rapid solvent exchange. (a) Reflectivity data was measured using three different aqueous solvent contrasts on the same sample. Curves shifted to show differences. (b) nSLD profile from simultaneous fitting of the reflectivity results using a box model. The slabs of homogenous density used to represent the system are delineated by vertical dashed lines.

TABLE 5.1 Best-Fit Parameters of the Box Model to a DMPC stBLM

Parameters	Fit Results
d of tether (Å)	$20.9^{+0.9}_{-0.4}$
vf of tether	$0.76^{0.02}_{-0.00}$
d of each lipid leaflet (Å)	$14.9^{+0.1}_{-0.6}$
vf of proximal chain	$1.00^{+0.00}_{-0.01}$
vf of distal chain	$1.00^{+0.00}_{-0.01}$
vf of distal headgroup	$0.66^{+0.09}_{-0.01}$
Global-interfacial roughness (Å)	$3.4^{+0.0}_{-0.5}$

d, thickness of layer; vf, volume fraction of a particular molecular component within a layer. Because the models were insensitive to the following quantities, these were taken as constants (not varied in the fit): thickness of the lipid headgroup, $d = 9.5$ Å; SLD of lipid chains, $\rho_n = -0.37 \times 10^{-6}$ Å^{-2}; SLD of lipid headgroup, $\rho_n = 1.8 \times 10^{-6}$ Å^{-2}; SLD of tether, $\rho_n = 1.2 \times 10^{-6}$ Å^{-2}. The interfacial RMS roughness was assumed to be identical for all interfaces. Errors are determined by the Monte Carlo resampling procedure.

different solvent contrasts: pure H_2O, pure D_2O, and CM4 (66% D_2O and 33% H_2O which matches to a SLD of 4×10^{-6} Å^{-2}). While producing distinct reflectivity curves, the underlying membrane structure is unperturbed by the different isotopic buffers. Simultaneous fitting of all three reflectivity spectra results in a best-fit "box" model presented in Figure 5.3b, where the correspondence of each layer to the molecular region that it represents is labeled on the figure. Three fit parameters are used to define each layer: the SLD (ρ), thickness (d), and the interfacial roughness (σ). The use of multiple solvent contrasts results in changing only ρ for regions where there is significant water penetration: the tether region, the lipid headgroups, and the aqueous reservoir. A fourth volume fraction (vf) parameter can then be defined for the tether and headgroup region that determines how much solvent occupies these layers. Invariance in ρ of the lipid hydrocarbon indicates defect-free membranes with no measurable water penetration into the lipid tail. Simultaneous fitting with multiple solvent contrasts is a powerful technique that reduces uncertainty in the fit parameters, ensures uniqueness of our model, and improves spatial resolution. A list of all the model parameters and their values for the tBLM membrane is given in Table 5.1.

5.4.2 Uncertainty Analysis

Uncertainty in fit parameters used to model reflectivity spectra arises from several sources: statistical error, maximum Q resolution, sample variance, and loss of phase information. For several of these factors, simultaneous fitting of multiple datasets using consistent substrate parameters and different aqueous contrast variations serve to greatly reduce parameter uncertainty. However, rigorous interpretation of reflectivity data using slab or other models require a measure of fit parameter confidence and the resulting variation in SLD profiles.

A Monte Carlo (MC) resampling technique [40] can be applied to determine both fit parameter confidence and parameter correlation [41]. In this approach, a large number, N (where $N \approx 1000$), of statistically independent sets of reflectivity data were created on the basis of the actual experimental data and their individual error bars. That is, for each measured data point, a new value was chosen randomly from a normal distribution centered around the measured value and with a variance based on the statistical error. Each new reflectivity spectra was then fit, generating a unique set of parameters and a SLD profile. Repeating this N number of times generates a distribution for each fit parameter as well as a family of SLD profiles, all of which are consistent with the experimental data. Statistical analysis can be applied to determine 1σ, 2σ, and 3σ confidence intervals. Figure 5.4 shows the results of MC analysis performed on a tether bilayer sample fit using a slab model. The distributions of lipid hydrophobic thickness and of the tether layer thickness, two of the fit parameters, are shown in the inset of Figure 5.4. The uncertainties for all parameters were calculated as the 95% percentile median and are given in Table 5.1. The resulting family of SLD profiles is represented as a broad band, where darker colors indicate well-defined regions of the profile. In this case, the variability in the bulk solvent SLD resulted in greater uncertainties in the headgroup and tether SLD since some volume fraction of solvent occupies these regions as well. Usually, the bulk solvent layer is fixed by experimental design, further reducing uncertainties in the SLD profile.

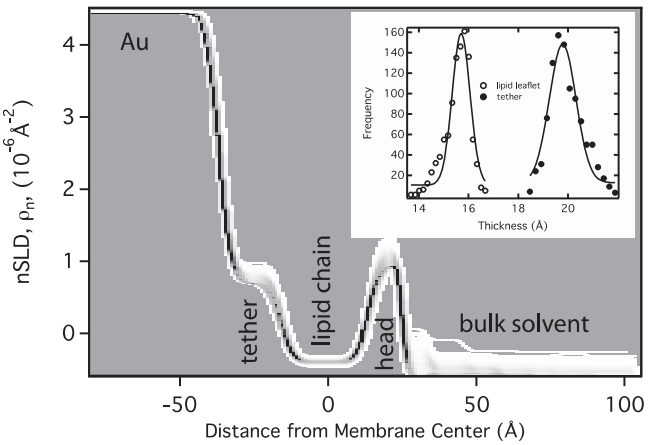

FIGURE 5.4 Results from Monte Carlo uncertainty analysis performed on reflectivity data from the tBLM in Fig. 5.3. The distributions of SLD profiles were superimposed where darker colors indicate regions of greater overlap between profiles. Inset: The distribution of values for two of the fit parameters, lipid leaflet, and tether thickness.

5.4.3 Composition Space Model

Box models have gotten a lot of "distance" with diverse application to metal films, polymers, and membrane protein assemblies. For complex molecular systems, however, they posses certain limitations that make interpreting the slab geometry in terms of the underlying molecular structure ambiguous. For instance, distinct chemical groups whose molecular volumes are thermally distributed and may significantly overlap along the membrane normal but not in the *xy*-plane of the film will be averaged in a box model. Hence, the distinction between the individual molecular distributions is lost in such a parameterization. Furthermore, the division of the real space into discreet slabs may impose artificial "step" boundaries in the SLD profile.

To overcome these drawbacks, composition-space techniques [42–47] parameterized based on submolecular components in the system have been developed. In these models, chemical groups and their distributed molecular volumes are represented individually and sum to the volumetric profile of the membrane film. Gaussian functions as well as hybrid boxcar and Gaussian functions have both been used to represent molecular distributions.

Adopting a similar philosophy, we recently developed a flexible and modular modeling technique that allows for direct fitting of reflectivity data to the underlying molecular architecture of the system [47]. However, in this model, molecular groups are represented by error functions, providing rigorous and efficient volume constraints and preventing unphysical fit results. Our continuous distribution (CD) model easily allows for the parameterization of multicomponent systems and isomorphic replacement of specific lipid species. As an example, a lipid bilayer consisting of 30% DMPS and 70 DMPC-d54 (all 54 hydrogens on the lipid tail were deuterated) was deposited onto Si/SiOx substrate. Figure 5.5a shows reflectivity profiles of the membrane layer with pure H_2O and pure D_2O solvent contrasts. The inset shows the fit using the molecular distribution model. The SLD of the two lipid leaflets vary significantly suggesting varying ratios of DMPC in each layer. Decomposition by the CD model (Fig. 5.5b) clearly finds that a greater percentage of DMPS partitions into the outer leaflet, hence lowering the total SLD of that region. Using physically meaningful volume and length values for the headgroups allowed for the resolution of the separate headgroup and tail distributions of the two lipid species.

The development of the CD model maximizes the information content extractable from reflectivity measurements with regards to membrane structure. In addition, the model can easily incorporate insertion of peptide and protein groups ensuring physically realistic redistribution of the lipid component volumes. If high-resolution X-ray or NMR measurements are available for the protein of interest, additional molecular detail with regard to protein orientation and amino acid interaction with the membrane can be determined, see the following section. Finally, representation of systems in compositional space allows for a straightforward joint refinement between X-ray and neutron reflectivity data.

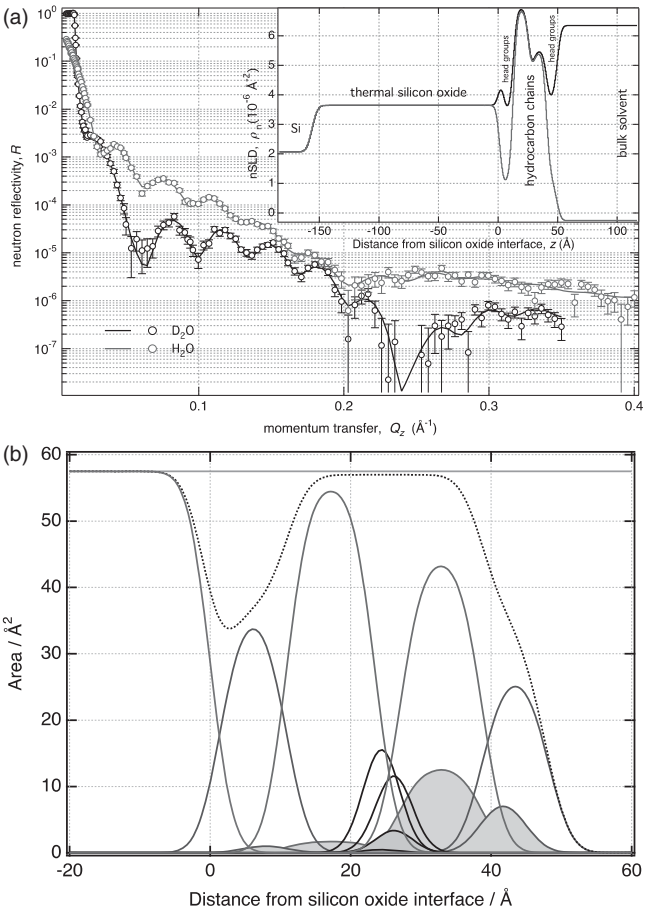

FIGURE 5.5 (a) Neutron reflectivity data and fit of a 70 mol% d54-DMPC: 30 mol% h-DMPS bilayer using two bulk solvent contrasts (H_2O, D_2O). Inset: nSLD profile obtained by the fit using the molecular distributions model. (b) Decomposition of the area profile into submolecular components as used by the model. Components of the proximal and distal leaflets are shown (blue: headgroups, red: hydrocarbon chains, black: terminal methyl groups). DMPS components are shown with filled background. (Adapted from Reference 47 with permission from the American Physical Society.) *See insert for a color representation of the figure.*

5.5 DETERMINING THE ORIENTATION AND INSERTION OF MEMBRANE-BOUND PROTEINS

Many peripheral membrane proteins exist in equilibrium between membrane-bound states and fractions soluble in the cellular cytoplasm. Membrane binding may be specifically targeted by unique lipid species or result from the confluence of several biochemical interactions, including electrostatic

attraction with charged lipids and insertion of hydrophobic moieties. The conformation and spatial orientation of peripheral membrane proteins with respect to the membrane surface is important for their function, yet identifying the membrane–protein interface from solution structures can prove difficult.

5.5.1 Example from the HIV-1 Gag Matrix (MA) Domain

The HIV-1 Gag viral protein is the central protein in mediating self-assembly of new virions in an infected host cell. Originally expressed in the cellular cytoplasm, the Gag protein eventually targets the surface of the plasma membrane. A 14-kDa N-terminal domain of Gag termed the matrix (MA) domain is responsible for membrane association [48]. It is thought that a bipartite mechanism is implicated in both membrane association and the selectivity for the plasma membrane. This mechanism includes a hydrophobic myristate anchor that is cotranslationally attached to the N-terminus of the protein and is believed to insert into the membrane [49–51]. In addition, a patch of basic residues forms attractive electrostatic interactions with anionic membrane lipids [50, 52, 53]. However, the structure and orientation of the MA domain on fluid plasma membranes had not been resolved in these earlier studies.

The electrostatic contribution to MA binding was investigated by the structural characterization of the interaction of MA lacking the myristate group with a model membrane system using neutron reflectivity [33]. A stBLM system was used as the biomimetic membrane environment and was composed of 30% anionic phosphatidylserine (PS) lipids and 70% neutral phosphatidylcholine (PC) lipids, while lacking the full complexity of the HIV lipodome [54,55] it conferred a similar negative charge density to that found in the viral membrane. The membrane layer was deposited by rapid solvent exchange.

Figure 5.6a shows the NR of the neat lipid bilayer in H_2O and of the same bilayer upon incubation with MA at two different concentrations of 1 μM and 10 μM. The spectra with protein show significant differences from those of the neat bilayer, which increase monotonically with protein concentration (Fig. 5.6a, bottom). Data interpretation was performed in successive steps of refinement in representing the protein structure. These steps were: (i) the "1-box"' model: protein modeled as a single homogenous slab of SLD normal to the membrane plane. (ii) The "free-form" model: divides the protein into a series of smaller homogenous slabs (≈15 Å thick) allowed to vary independently, therefore not presupposing the SLD profile. (iii) In a further step of refinement, the NMR structure of the MA domain [56] was used to determine the protein SLD profile with the protein in a fixed orientation with respect to the membrane. In this case, the profile is derived from the ensemble average of the 20 structures provided by the NMR dataset.

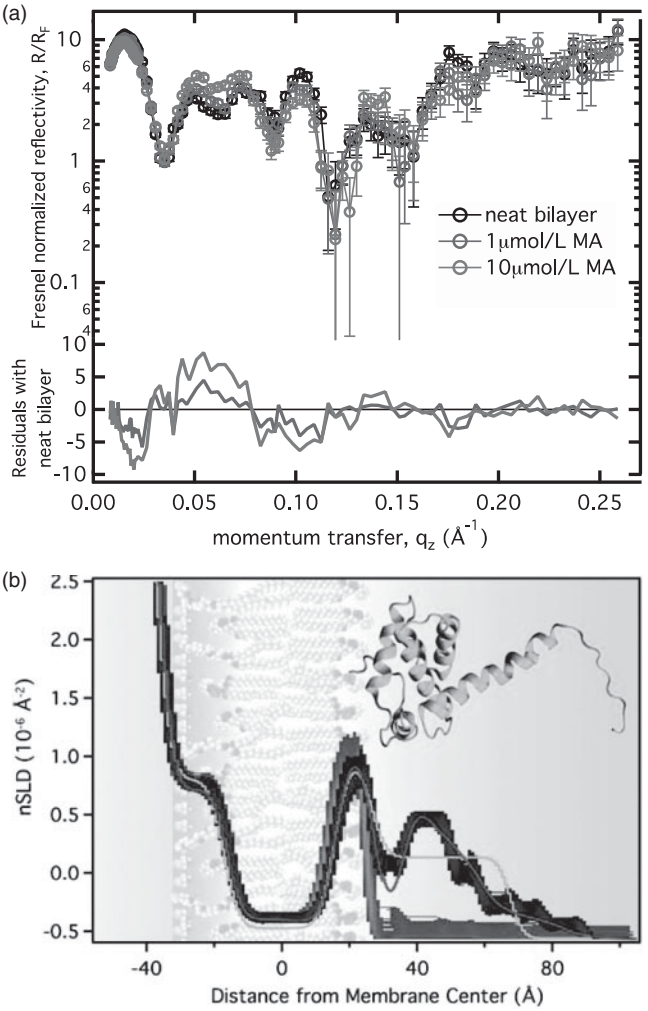

FIGURE 5.6 (a) NR of a stBLM with increasing concentrations of MA in H_2O-based aqueous buffer. The reflection spectra are normalized to the Fresnel reflectivity (i.e., the reflectivity of a neat Si–buffer interface without interfacial roughness) in order to emphasize the interference patterns due to the interfacial structures. The bottom plot shows the error-weighted residuals of the stBLM reflectivities with protein to the reflectivity without protein. (b) SLD profiles of 10 μM MA samples using models of increasing refinement to fit the protein layer. (i) 1-box model: yellow line, single slab of homogenous SLD; (ii) free-form model: dark blue line, six slabs were allowed to vary independently generating the protein profile. The wide bands represent 95% confidence interval from MC resampling analysis. The neat stBLM was also fit by the MC analysis and is shown in the gray line. (iii) NMR-model: red line, average over 20 solution NMR structures to generate SLD profile. Surface coverage and z-position were the only fit parameters. (Reproduced from Reference 33 with permission from the Biophysical Society.) *See insert for a color representation of the figure.*

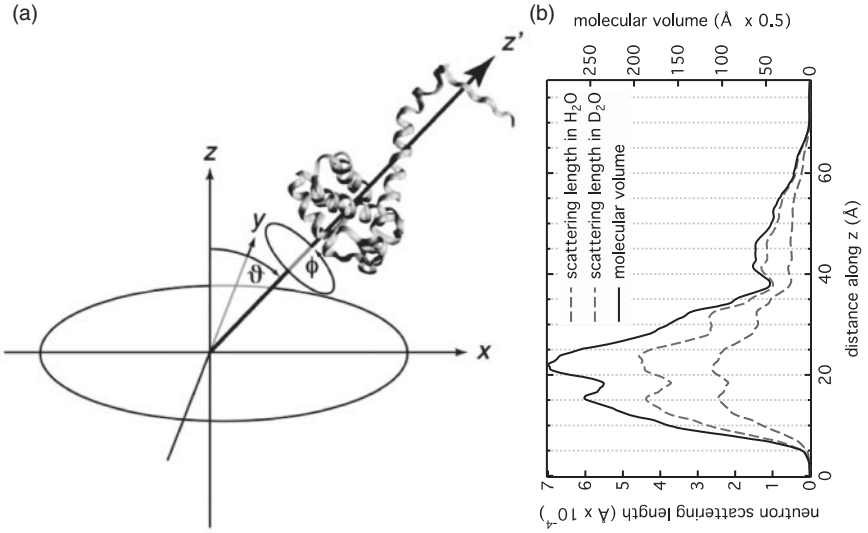

FIGURE 5.7 (a) Depiction of Euler angles (θ, ϕ) that define protein orientation on the membrane. (b) Example of neutron scattering length and molecular volume profiles calculated along membrane normal, z, for a given orientation.

The resulting SLD models are shown in Figure 5.6b. The 1-box model (yellow line) has dimensions of 40 Å and appears to approximate an average of the free-form model (dark blue line), truncating the tail region of the free-form scattering profile. The width of the free-form profile represents the 95% confidence limits, determined by the Monte Carlo uncertainty analysis discussed previously. Clearly, the distinct shape of the profile is significant and the observed density is well above the uncertainty in our pure lipid model (gray line). The reflectivity results find a larger density of protein proximal to the membrane surface with a 20 Å tail extending out from this region.

A molecular interpretation of the free-form profile is only possible using the NMR structure refinement model. Choosing the putative membrane interface, only the surface coverage of protein and the insertion depth into the membrane were allowable fit parameters. The results suggest that the dense region adjacent to the membrane corresponds well to the core of the MA protein and the tail to a C-terminus α-helix and adjacent flexible amino acid stretch.

5.5.2 Determining Protein Orientation

The qualitative agreement between the free-form profile and the NMR-based SLD profile encouraged further refinement of MA orientation on the membrane. To parameterize the MA orientation with respect to the membrane, rigid body rotations of the NMR structures were performed around the center of mass of the protein. Euler angles ϑ and ϕ define, respectively, the polar rotation of a local axis, z', associated with the protein against the surface normal, z, and the azimuthal rotation of the protein around z' (Fig. 5.7a). As a starting point that defines $(\vartheta, \phi) = (0^\circ, 0^\circ)$, the putative binding orientation suggested by Hill et al. [57] was used. For each rigid body rotation, the SL and molecular volume profile along the bilayer normal was calculated (Fig. 5.7b). The Euler angles were then made fit variables along with the penetration depth, z position, of the protein into the membrane and the protein surface coverage. Monte Carlo uncertainty analysis provided a distribution of values for all fit parameters including orientation and depth penetration.

The Euler angle distribution is depicted as a contour plot in Figure 5.8a that shows contour lines for the 68.2%, 95.4%, and 99.6% confidence intervals, each representing the probability that the protein orientation which best models the data is within that contour line. The probability densities at any given orientation are color coded using a linear scale "heat" plot. The 68.2% contour line, representing the most probable orientations, is tightly centered at approximately (20^{o}, 110^{o}). The 95.4% confidence contour defines an approximate 20^{o} tolerance that includes the (0^{o}, 0°) orientation. Superimposing the rigid body rotations of the NMR structures, Figure 5.8b gives a visual impression of the orientation uncertainty. The ribbon representations of the protein have been color coded to match Figure 5.8a. It can be seen that the distribution of protein orientations consistent with the experimental results are those in which the MA domain maintains an upright profile with the N-terminus near the membrane surface.

The average penetration depth of the MA protein for all fits within the 95.4% contour was –4.8 $\pm$ 1.7 Å relative to the headgroup-solvent boundary. As shown in Figure 5.9,

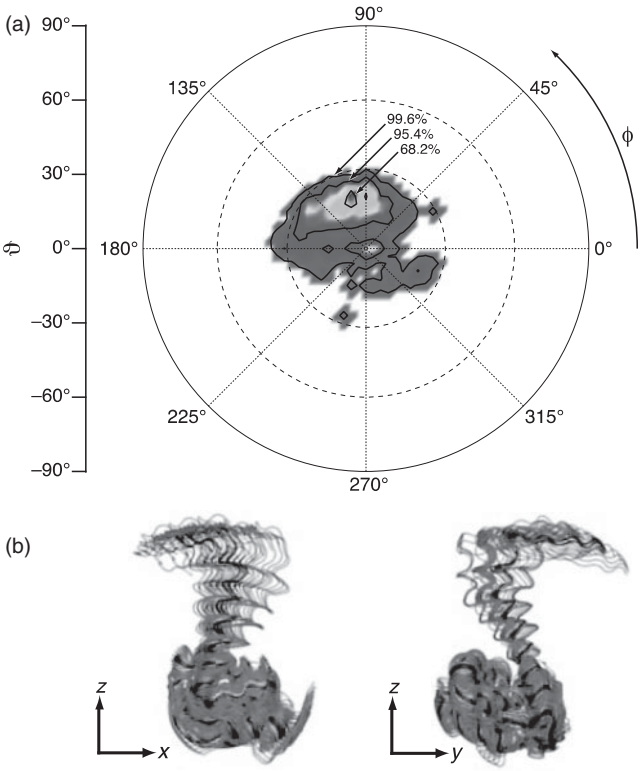

FIGURE 5.8 (a) Most probable orientation of membrane-bound MA determined from MC resampling analysis and NMR-based SLD profiles. The colored "heat" plot is linearly scaled to the probability density of Monte Carlo resampled fits that resulted in a particular orientation, where red represents the highest density and violet the lowest. The 68.2% contour shows that a majority of fits fall within a narrow region localized around $(\vartheta,\phi) = (20,110)$. (b) Projections of protein orientations onto the *x,z*-plane (left) and *y,z*-plane (right). The membrane surface (not shown) is at the *x,y*-plane. Protein structures are color coded to match the contour plot of panel a. (Reproduced from Reference 33 with permission from the Biophysical Society.) *See insert for a color representation of the figure.*

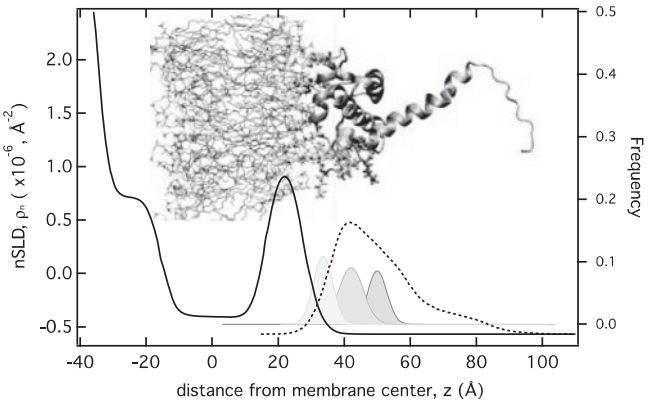

FIGURE 5.9 Most likely MA protein nSLD profile based on NR modeling to obtain protein orientation and penetration depth into the membrane. A molecular model of MA bound to the membrane is overlayed on the plot. Basic residues in the protein were divided into three groups based on proximity to the membrane interface and highlighted in the molecular model. The number density distributions of these residues based on the uncertainty in the orientation and penetration parameter are shown on the plot as filled profiles. (Reproduced from Reference 33 with permission from the Biophysical Society.) *See insert for a color representation of the figure.*

this is consistent with a surface-associated protein. At this penetration depth, backbone atoms do not enter the membrane region, but amino acid side chains are still able to peripherally insert into the headgroup layer. Figure 5.9 (inset) provides a molecular depiction of the MA protein on a membrane surface. Basic residues that are potentially important for membrane association are highlighted.

This work demonstrates the ability of NR to characterize the lipid-bound state of membrane proteins in molecular details. Although intrinsically a low-resolution method, the information content of the NR results can be dramatically enhanced by refinement of the data using atomistic detail from NMR or X-ray structures of the protein. This methodology yields structural details of molecular complexes at the membrane interface that could not be determined by either of the structural characterization techniques alone.

5.6 CONFORMATIONAL CHANGES OF PROTEINS ON THE MEMBRANE

Another powerful application of NR is the direct observation of structural changes in proteins in response to biochemical interactions. Protein interaction with cofactors is possible in physiologically relevant environments, that is, associated with fluid lipid bilayers and in proper aqueous buffer. Measurements performed on the full HIV-1 Gag construct highlight the application of NR to identify interactions that induce conformational changes necessary for protein function.

The HIV-1 Gag protein has a multidomain architecture consisting of, from the N- to C-terminus, a matrix (MA) domain, a capsid (CA) domain, and a nucleocapsid (NC) domain (see molecular picture in Figure 5.10c). Long flexible amino acid linkers without resolvable structure join the domains. As previously discussed, the MA region is responsible for membrane targeting of the Gag protein. Lateral protein–protein interactions on the membrane are largely or exclusively a function of the CA domain, while the NC domain is principal in the incorporation of the viral genome into the assembling virion. Newly formed viral particles arise by budding from the cell membrane and result in an outer lipid vesicle coat, with Gag and other viral proteins organized inside.

Individual domain subunits of Gag have been resolved to atomic resolution by X-ray crystallography and NMR. Due to its flexible nature, the full-length protein has defied high-resolution methods. Therefore, current structural knowledge of the complete Gag construct has been derived from

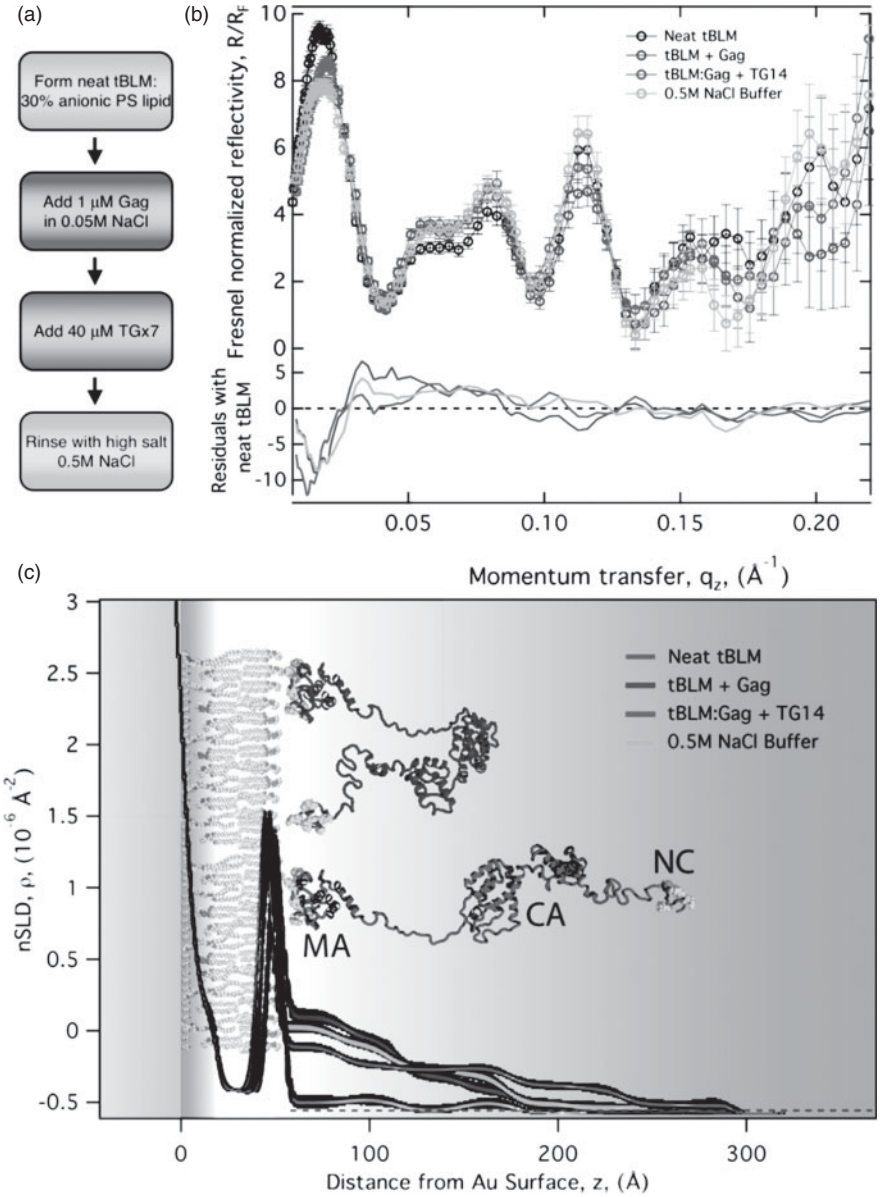

FIGURE 5.10 (a) The sequence of measurements performed *in situ* on the reflectometry instrument. The steps are as follows: (i) Formation of a complete tBLM. (ii) Binding WT Gag (buffer: 0.05 M NaCl, 0.001 M $NaPO_4$, 5 mM TCEP, pH 7.4). (iii) Binding of TG $\times$ 7 DNA to the Gag protein layer. (iv) Disassociation of TG $\times$ 7 using a high-ionic strength buffer (same as binding buffer except 0.5 M NaCl). (b) Resulting reflectivity spectra for the series of measurements showing the pure H_2O buffer data only. Differences in reflectivity from the neat tBLM condition are given as residuals in the bottom of the panel. (c) nSLD profile of the membrane and Gag determined by a free-form model. Line widths represent the 95% confidence limits. The inset showing WT Gag cartoons are illustrative models of protein conformations consistent with the overall dimensions determined by reflectivity. (Reproduced from Reference 60 with permission from Academic Press.) *See insert for a color representation of the figure.*

small-angle neutron scattering (SANS) and cryo-electron microscopy. SANS studies indicated that the Gag protein adopted conformations with a mean particle radius, $Rg \approx 35$ Å when in solution [58]. Modeling the conformational variability in the flexible linkers found only compact structures of this protein, structures where the N-terminal MA domain and C-terminal NC domain were proximal to each other, matched with the scattering data. However, cryo-electron microscopy of immature virus particles resolved an extended Gag protein, rod like and radially pointing from the viral membrane

by approximately 200 Å [59]. Thus, it was apparent that large structural changes in the protein were concomitant with assembly though molecular mechanisms were not known.

Using NR, we sought to capture intermediate stages of Gag assembly on the membrane and to identify interactions that influence protein conformation [60]. Gag binding was studied on a stBLM composed of 30% anionic phosphatidylserine (PS) and 70% neutral lipids. As we showed in the previous section, this lipid composition was capable of binding MA domain to the membrane in an orientation that is consistent with proper Gag assembly.

A sequence of experiments outlined in Figure 5.10a were conducted to investigate the structure of Gag protein on the model membrane. Initially, the neat negatively charged bilayer was formed and measured by NR to ensure a defect-free, $>$ 90% complete, membrane over the wafer surface. Gag was then introduced into the aqueous phase, where it bound to the membrane. The bound protein was then incubated with the TG $\times$ 7 to observe the effect of nucleic acid on the membrane-bound protein. Finally, the TG $\times$ 7 construct was removed from the Gag molecules by flushing the sample cell with a high-salt (0.5 M NaCl) buffer.

Changes in the reflectivity spectra indicate both binding of Gag and modulation of protein conformation due to the different experimental conditions. Figure 5.10b shows the reflectivity profiles measured in the H_2O aqueous buffer contrast. Differences between the Gag protein conditions and the neat bilayer are shown as residuals in the bottom part of Figure 5.10b. For each experimental condition, reflectivity spectra were measured using three separate isotopic aqueous buffer contrasts (pure H_2O, a 1:2 H_2O:D_2O mixture and pure D_2O), resulting in the simultaneous fitting of 12 different datasets.

Interpretation of the reflectivity profiles for these complex systems was performed using the "free-form" box model as described in the previous section to represent the protein layer. The nSLD profiles are shown in Figure 5.10c where line widths are 95% confidence limits determined by Monte Carlo error analysis.

The nSLD profile for the neat bilayer is shown in Figure 5.10c (black line) and indicates a nearly defect-free membrane, showing only bulk solvent after the outer-leaflet headgroup region. When Gag was introduced, it formed a protein layer with total dimensions of $\approx$90 Å, Figure 5.10c (blue line). The subsequent introduction of single-stranded TG $\times$ 7 DNA causes a shift in Gag dimension, extending $\approx$190 Å, Figure 5.10c (red line). These dimensions agree well with Gag protein dimensions in the immature virion [59]. A nearly complete recovery of the compact state of Gag was induced by the high-salt rinse, Figure 5.10c (green line). The inset showing Gag cartoons structures are illustrative models of possible protein conformations that are consistent with the overall dimensions determined by reflectivity. The SLD profile is likely an average of an ensemble of Gag conformations due to the intrinsically disordered regions between the structured domains.

It would appear from these results that HIV-1 Gag is incapable of proper particle assembly *in vivo* until it reaches the plasma membrane and is in contact with RNA. Further work is needed to dissect the temporal sequence of the events needed in Gag extension and subsequent assembly. Furthermore, molecular simulations or other algorithms for conformational sampling [61] that generate the ensemble of states in disordered protein regions may provide a mechanism for matching atomic structural information to the envelope SLD profiles generated by NR [20]. Nonetheless, these experiments illustrate the formidable capabilities of reflectivity to determine molecular mechanisms that drive protein conformational change in physiologically relevant fluid membrane environments.

5.7 CONCLUSION

In the past decade, tremendous progress in the application of neutron reflectivity to proteins at membrane interfaces have been made. These advances have been across the board not only in instrumentation but also in sample environment and data interpretation. Continuing efforts at neutron facilities and academic research laboratories promise many more improvements in the future. High-intensity spallation sources will push resolution limits with higher neutron flux. Equally exciting are the developments of a chromatic beam reflectometer at the NIST Center for Neutron Research which will take advantage of the full bandwidth of the neutron beam, not only improving resolution but potentially allowing for time resolved NR.

Just as important is the progress many protein-labeling facilities are making in protocols for specific deuteration of protein domains and residues. Though a biochemically difficult problem, the information content from neutron scattering measurements will be dramatically increased by specific labeling, providing new molecular insights into protein conformational reorganization as it relates to function. In addition, continuing to integrate structural information from many different protein metrologies, especially those that can probe lateral protein organization, will produce accurate multiscale models of larger supramolecular assemblies.

The potential of membrane proteins as therapeutic targets has resulted in major efforts to study these complicated systems. Continuing developments in NR will therefore translate well into real-life applications and directly benefit industries in the biotechnology sector.

REFERENCES

1. Kobilka BK. G protein coupled receptor structure and activation. *Biochim Biophys Acta* 2007;1768(4):794–807.

2. Colombini M. A candidate for the permeability pathway of the outer mitochondrial membrane. *Nature* 1979;279(5714):643–645.
3. Deshaies RJ, Sanders SL, Feldheim DA, Schekman R. Assembly of yeast sec proteins involved in translocation into the endoplasmic-reticulum into a membrane-bound multisubunit complex. *Nature* 1991;349(6312):806–808.
4. Spearman P, Wang JJ, Vander Heyden N, Ratner L. Identification of human immunodeficiency virus type 1 Gag protein domains essential to membrane binding and particle assembly. *J Virol* 1994;68(5):3232–3242.
5. Milhiet PE, Gubellini F, Berquand A, Dosset P, Rigaud JL, Le Grimellec C, Lévy D. High-resolution AFM of membrane proteins directly incorporated at high density in planar lipid bilayer. *Biophys J* 2006;91(9):3268–3275.
6. Cuello LG, Cortes DM, Perozo E. Molecular architecture of the KvAP voltage-dependent K + channel in a lipid bilayer. *Science* 2004;306(5695):491–495.
7. Thompson LK. Solid-state NMR studies of the structure and mechanisms of proteins. *Curr Opin Struct Biol* 2002;12(5):661–669.
8. Zhang W, Chipman PR, Corver J, Johnson PR, Zhang Y, Mukhopadhyay S, Baker TS, Strauss JH, Rossmann MG, Kuhn RJ. Visualization of membrane protein domains by cryo-electron microscopy of dengue virus. *Nat Struct Biol* 2003;10(11):907–912.
9. Long SB, Campbell EB, MacKinnon R. Crystal structure of a mammalian voltage-dependent Shaker family K + channel. *Science* 2005;309(5736):897–903.
10. Wacklin HP. Neutron reflection from supported lipid membranes. *Curr Opin Colloid Interface Sci* 2010;15(6):445–454.
11. Weygand M, Wetzer B, Pum D, Sleytr UB, Cuvillier N, Kjaer K, Howes PB, Lösche M. Bacterial S-layer protein coupling to lipids: X-ray reflectivity and grazing incidence diffraction studies. *Biophys J* 1999;76(1):458–468.
12. Sinha SK, Sirota EB, Garoff S, Stanley HB. X-ray and neutron-scattering from rough surfaces. *Phys Rev B* 1988;38(4):2297–2311.
13. Jablin MS, Zhernenkov M, Toperverg BP, Dubey M, Smith HL, Vidyasagar A, Toomey R, Hurd AJ, Majewski J. In-plane correlations in a polymer-supported lipid membrane measured by off-specular neutron scattering. *Phys Rev Lett* 2011;106(13):138101.
14. Krueger S, Meuse CW, Majkrzak CF, Dura JA, Berk NF, Tarek M, Plant, AL. Investigation of hybrid bilayer membranes with neutron reflectometry: probing the interactions of melittin. *Langmuir* 2001;17(2):511–521.
15. Berk NF, Majkrzak CF. Wavelet analysis of neutron reflectivity. *Langmuir* 2003;19(19):7811–7817.
16. Majkrzak CF, Berk NF, Perez-Salas UA. Phase-sensitive neutron reflectometry. *Langmuir* 2003;19(19):7796–7810.
17. Johnson SJ, Bayerl TM, Weihan W, Noack H, Penfold J, Thomas RK, Kanellas D, Rennie AR, Sackmann E. Coupling of spectrin and polylysine to phospholipid monolayers studied by specular reflection of neutrons. *Biophys J* 1991;60(5):1017–1025.
18. Vaknin D, Kjaer K, Ringsdorf H, Blankenburg R, Piepenstock M, Diederich A, Losche M. X-ray and neutron reflectivity studies of a protein monolayer adsorbed to a functionalized aqueous surface. *Langmuir* 1993;9(5):1171–1174.
19. Weygand M, Kjaer K, Howes PB, Wetzer B, Pum D, Sleytr UB, Losche M. Structural reorganization of phospholipid headgroups upon recrystallization of an S-layer lattice. *J Phys Chem B* 2002;106(22):5793–5799.
20. Kent, MS, Murton JK, Sasaki DY, Satija S, Akgun B, Nanda H, Curtis JE, Majewski J, Morgan CR, Engen JR. Neutron reflectometry study of the conformation of HIV Nef bound to lipid membranes. *Biophys J* 2010;99(6):1940–1948.
21. Meuse CW, Krueger S, Majkrzak CF, Dura JA, Fu J, Connor JT, Plant AL. Hybrid bilayer membranes in air and water: infrared spectroscopy and neutron reflectivity studies. *Biophys J* 1998;74(3):1388–1398.
22. Smith MB, McGillivray DJ, Genzer J, Lösche M, Kilpatrick PK. Neutron reflectometry of supported hybrid bilayers with inserted peptide. *Soft Matter* 2010;6(5):862–865.
23. Johnson SJ, Bayerl TM, McDermott DC, Adam GW, Rennie AR, Thomas RK, Sackmann E. Structure of an adsorbed dimyristoylphosphatidylcholine bilayer measured with specular reflection of neutrons. *Biophys J* 1991;59(2):289–294.
24. Koenig BW, Kruger S, Orts WJ, Majkrzak CF, Berk NF, Silverton JV, Gawrisch K. Neutron reflectivity and atomic force microscopy studies of a lipid bilayer in water adsorbed to the surface of a silicon single crystal. *Langmuir* 1996;12(5):1343–1350.
25. Blodgett KB, Langmuir I. Built-up films of barium stearate and their optical properties. *Phys Rev* 1937;51(11):0964–0982.
26. Cornell BA, Braach-Maksvytis VL, King LG, Osman PD, Raguse B, Wieczorek L, Pace RJ. A biosensor that uses ion-channel switches. *Nature* 1997;387(6633):580–583.
27. Wong JY, Majewski J, Seitz M, Park CK, Israelachvili JN, Smith GS. Polymer-cushioned bilayers. I. A structural study of various preparation methods using neutron reflectometry. *Biophys J* 1999;77(3):1445–1457.
28. Smith HL, Jablin MS, Vidyasagar A, Saiz J, Watkins E, Toomey R, Hurd AJ, Majewski J. Model lipid membranes on a tunable polymer cushion. *Phys Rev Lett* 2009;102(22):228102.
29. Garg S, Rühe J, Lüdtke K, Jordan R, Naumann CA. Domain registration in raft-mimicking lipid mixtures studied using polymer-tethered lipid bilayers. *Biophys J* 2007;92(4):1263–1270.
30. Naumann R, Schiller SM, Giess F, Grohe B, Hartman KB, Karcher I, Koper I, Lubben J, Vasilev K, Knoll W. Tethered lipid bilayers on ultraflat gold surfaces. *Langmuir* 2003;19(13):5435–5443.
31. McGillivray DJ, Valincius G, Vanderah DJ, Febo-Ayala W, Woodward JT, Heinrich F, Kasianowicz JJ, Lösche M. Molecular-scale structural and functional characterization of sparsely tethered bilayer lipid membranes. *Biointerphases* 2007;2(1):21–33.
32. McGillivray DJ, Valincius G, Heinrich F, Robertson JW, Vanderah DJ, Febo-Ayala W, Ignatjev I, Lösche M, Kasianowicz JJ. Structure of functional *Staphylococcus aureus* α-hemolysin

channels in tethered bilayer lipid membranes. *Biophys J* 2009;96:1547–1553.

33. Nanda H, Datta SA, Heinrich F, Lösche M, Rein A, Krueger S, Curtis JE. Electrostatic interactions and binding orientation of HIV-1 matrix studied by neutron reflectivity. *Biophys J* 2010;99(8):2516–2524.
34. Shenoy S, Moldovan R, Fitzpatrick J, Vanderah DJ, Deserno M, Lösche M. In-plane homogeneity and lipid dynamics in tethered bilayer lipid membranes (tBLMs). *Soft Matter* 2010;6(6):1263–1274.
35. Majkrzak CF, Berk NF, Krueger S, Dura JA, Tarek M, Tobias D, Silin V, Meuse CW, Woodward J, Plant AL. First-principles determination of hybrid bilayer membrane structure by phase-sensitive neutron reflectometry. *Biophys J* 2000;79(6):3330–3340.
36. Perez-Salas UA, Faucher KM, Majkrzak CF, Berk NF, Krueger S, Chaikof EL. Characterization of a biomimetic polymeric lipid bilayer by phase sensitive neutron reflectometry. *Langmuir* 2003;19(19):7688–7694.
37. King GI, White SH. Determining bilayer hydrocarbon thickness from neutron-diffraction measurements using strip-function models. *Biophys J* 1986;49(5):1047–1054.
38. Franks NP, Melchior V, Kirshner DA, Caspar DL. Structure of myelin lipid bilayers - changes during maturation. *J Mol Biol* 1982;155(2):133–153.
39. Parratt LG. Surface studies of solids by total reflection of X-rays. *Phys. Rev.* 1954;95:359–369.
40. Press WH, and Numerical Recipes Software (Firm). *Numerical Recipes*. Cambridge: Cambridge University Press; 1996, p. 1.
41. Heinrich F, Ng T, Vanderah DJ, Shekhar P, Mihailescu M, Nanda H, Lösche M. A new lipid anchor for sparsely-tethered bilayer lipid membranes. *Langmuir* 2009;25:4219–4229.
42. Wiener MC, White SH. Fluid bilayer structure determination by the combined use of X-ray and neutron-diffraction .2. Composition-space refinement method. *Biophys J* 1991;59(1):174–185.
43. Wiener MC, White SH. Fluid bilayer structure determination by the combined use of X-ray and neutron-diffraction. 1. Fluid bilayer models and the limits of resolution. *Biophys J* 1991;59(1):162–173.
44. Schalke M, Krüger P, Weygand M, Lösche M. Submolecular organization of DMPA in surface monolayers: beyond the two-layer model. *Biochim Biophys Acta* 2000;1464(1):113–126.
45. Schalke M, Losche M. Structural models of lipid surface monolayers from X-ray and neutron reflectivity measurements. *Adv Colloid Interface Sci* 2000;88(1–2):243–274.
46. Kucerka N, Nagle JF, Sachs JN, Feller SE, Pencer J, Jackson A, Katsaras J. Lipid bilayer structure determined by the simultaneous analysis of neutron and X-ray scattering data. *Biophys J* 2008;95(5):2356–2367.
47. Shekhar P, Nanda H, Lösche M, Heinrich F. Continuous distribution model for the investigation of complex molecular architectures near interfaces with scattering techniques. *J Appl Phys* 2011;110:102216.
48. Bukrinskaya A. HIV-1 matrix protein: a mysterious regulator of the viral life cycle. *Virus Res* 2007;124(1–2):1–11.
49. Bryant M, Ratner L. Myristoylation-dependent replication and assembly of human immunodeficiency virus 1. *Proc Natl Acad Sci USA* 1990;87(2):523–527.
50. Zhou WJ, Parent LJ, Wills JW, Resh MD. Identification of a membrane binding domain within the amino-terminal region of human immunodeficiency virus type 1 Gag protein which interacts with acidic phospholipids. *J Virol* 1994;68(4):2556–2569.
51. Spearman P, Horton R, Ratner L, Kuli-Zade I. Membrane binding of human immunodeficiency virus type 1 matrix protein in vivo supports a conformational myristyl switch mechanism. *J Virol* 1997;71(9):6582–6592.
52. Freed EO, Englund G, Martin MA, Role of the basic domain of human immunodeficiency virus type 1 matrix in macrophage infection. *J Virol* 1995;69(6):3949–3954.
53. Ono A, Orenstein JM, Freed EO. Role of the Gag matrix domain in targeting human immunodeficiency virus type 1 assembly. *J Virol* 2000;74(6):2855–2866.
54. Brügger B, Glass B, Haberkant P, Leibrecht I, Wieland FT, Kräusslich HG. The HIV lipidome: a raft with an unusual composition. *Proc Natl Acad Sci USA* 2006;103(8):2641–2646.
55. Chan R, Uchil PD, Jin J, Shui G, Ott DE, Mothes W, Wenk MR. Retroviruses human immunodeficiency virus and murine leukemia virus are enriched in phosphoinositides. *J Virol* 2008;82(22):11228–11238.
56. Saad JS, Miller J, Tai J, Kim A, Ghanam RH, Summers MF. Structural basis for targeting HIV-1 Gag proteins to the plasma membrane for virus assembly. *Proc Natl Acad Sci USA* 2006;103(30):11364–11369.
57. Hill CP, Worthylake D, Bancroft DP, Christensen AM, Sundquist WI. Crystal structures of the trimeric human immunodeficiency virus type 1 matrix protein: implications for membrane association and assembly. *Proc Natl Acad Sci USA* 1996;93(7):3099–3104.
58. Datta SAK, Curtis JE, Ratcliff W, Clark PK, Crist RM, Lebowitz J, Krueger S, Rein A. Conformation of the HIV-1 gag protein in solution. *J Mol Biol* 2007;365(3):812–824.
59. Fuller SD, Wilk T, Gowen BE, Kräusslich HG, Vogt VM. Cryo-electron microscopy reveals ordered domains in the immature HIV-1 particle. *Curr Biol* 1997;7(10):729–738.
60. Datta SAK, Heinrich F, Raghunandan S, Krueger S, Curtis JE, Rein A, Nanda H. HIV-1 gag extension: conformational changes require simultaneous interaction with membrane and nucleic acid. *J Mol Biol* 2011;406(2):205–214.
61. Curtis JE, Raghunandan S, Nanda H, Krueger S. SASSIE: a program to study intrinsically disordered biological molecules and macromolecules and macromolecular assemblies using experimental scattering restraints. *Comput Phys Commun* 2012;183(2):382–389.